ChemCatChem

ChemCatChem
Chemistry Europe
European Chemical Societies Publishing

RESEARCH ARTICLE OPEN ACCESS

Engineered Tantalum–Iridium Oxide Nanoparticles via High-Temperature Calcination for Oxygen Evolution Catalysis

Marko Malinovic[1] | Moritz Geuß[2] | Paul Paciok[3] | Jisik Choi[1] | Huize Wang[2] | Souriddha Sanyal[1] | Philipp Pfeifer[1] | Serhiy Cherevko[2] | Marc Heggen[3] | Marc Ledendecker[1,2]

[1]Technical University Munich, Campus Straubing, Sustainable Energy Materials, Straubing, Germany | [2]Helmholtz Institute Erlangen-Nürnberg For Renewable Energy, Forschungszentrum Jülich GmbH, Erlangen, Germany | [3]Ernst Ruska-Centre (ER-C-1), Forschungszentrum Jülich GmbH, Jülich, Germany

Correspondence: Marko Malinovic (marko.malinovic@tum.de) | Marc Ledendecker (marc.ledendecker@tum.de)

Received: 2 October 2025 | **Revised:** 28 November 2025 | **Accepted:** 30 December 2025

Keywords: catalysis | iridium oxide | nanoparticles | oxygen evolution reaction | polymer electrolyte membrane water electrolysis | stability | Tantalum tantalum oxide

ABSTRACT

Sustainable hydrogen production via low-temperature water electrolysis is key to advancing the hydrogen economy, with polymer electrolyte membrane water electrolysis (PEM-WE) as a central technology. However, sluggish oxygen evolution reaction (OER) kinetics at the anode limit PEM-WE efficiency. Iridium-based catalysts remain the benchmark due to their balance of activity and stability under harsh conditions, though iridium scarcity necessitates designs with reduced Ir content. Here, we report a highly active and stable OER catalyst based on TaO_x–IrO_2 nanoparticles synthesized via a reverse microemulsion method and calcined at 800°C. Encapsulation in silica nanoreactors enabled precise control over particle size and crystallinity during thermal treatment. The TaO_x–IrO_2 catalyst achieves a mass activity of 619 ± 93 mA mg_{Ir}^{-1} at 1.55 V_{RHE}, outperforming commercial IrO_2 by a factor of 2.5 and bare IrO_2 synthesized under identical conditions. While TaO_x is electrochemically inactive, it shows exceptional dissolution resistance. The intrinsic stability of TaO_x–IrO_2, expressed via the S-number, exceeds that of commercial IrO_2 and matches bare IrO_2 calcined at 600°C. These results highlight TaO_x–IrO_2 as a promising OER catalyst, combining enhanced activity with notable stability, and support the development of durable, efficient catalysts for PEM-WE.

1 | Introduction

Low-temperature water electrolysis technologies hold a central role in sustainable hydrogen generation and will have a significant impact on the further advancement of the hydrogen economy [1]. Besides, mature alkaline electrolysis, with a 40% forecasted green hydrogen market coverage, commercialized polymer electrolyte membrane water electrolysis (PEM-WE) promises to be the key to scaling up the green hydrogen production capacity [2, 3]. The full realization of the PEM-WE potential is, among other factors, mainly impeded by a notable increase in the electrolyzer's overpotential stemming from the slow kinetics of the anodic oxygen evolution reaction (OER) [4–6]. The selection of catalyst material capable of catalyzing OER while maintaining suitable resilience towards dissolution is almost exclusively limited to iridium-based catalysts, given the rigorous OER operating conditions of high potential (> 1.4 V_{RHE}) and low pH arising from the perfluorosulfonic-based membrane [7]. Specifically, the oxide form of iridium is particularly suited to catalyze the OER, where a structurally ordered iridium oxide (IrO_2) is known for enhanced resistance to dissolution under OER conditions and respectable OER activity, compared to highly

active amorphous (hydrous) iridium oxide (IrO_x) that is more prone to dissolution [8, 9]. Regarded among the rarest elements on earth, various approaches have been suggested to circumvent the iridium shortage while simultaneously maximizing the catalyst's activity toward OER including nanostructuring, dynamic IrO_x surface reconstruction [10], doping of IrO_x [11], or mixing IrO_x nanoparticles with materials based on earth-abundant elements [12]. Especially the latter approach would potentially enable noticeable reduction in iridium's packing density, thus enable generation of sufficiently thick electrodes, necessary for PEM-WE scale-up. [4, 5, 13] To realize this strategy, introducing a stable, high surface area support material with sufficient conductivity is of major importance. [14, 15] Here, the biggest progress is made with pristine TiO_2/TiO_x [16] and SnO_2 [17] or their less stable but more conductive doped counterparts M-TiO_2 (M═Nb, Ta, V etc.), M—SnO_2, (M═Sb, In, F etc.) [18–21].The potential application of thermodynamically stable transition metal oxides such as Ta_2O_5, Nb_2O_5 has also been in research focus [14, 22–24]. One example is mass-selected $Ir_{0.1}Ta_{0.9}O_{2.45}$ nanoparticles smaller than 2 nm exhibit a mass activity of 1.2 ± 0.5 A mg_{Ir}^{-1} at an overpotential of 320 mV, which is about two times higher than that of mass-selected IrO_2. However, the synthesis remains constrained to a small scale due to the ultrahigh-vacuum cluster source technique used [25].

The favorable interaction between inactive transition metal oxide and OER active material, yielded active OER catalysts, but also showed a stabilizing effect and mitigated precious metal dissolution of usually less stable hydrous IrO_x [13, 26].

Böhm et al. [27] addressed the often-overlooked aspect of catalyst stability, demonstrating enhanced corrosion resistance of hydrous IrO_x supported on titania through crystallization achieved by controlled thermal oxidation up to 375°C. This approach not only improved the catalyst's stability but also its conductivity. However, a further increase in temperature to 400°C induced uncontrolled particle growth and a change in morphology, consequently diminishing the positive effect of thermal treatment on the catalyst's stability and conductivity. This outcome proved the hardship of preserving the high surface area of structurally ordered IrO_2.

Here, we present an OER catalyst based on an iridium-tantalum oxide nanoparticles (TaO_x-IrO_2) generated in a reverse microemulsion. Encapsulation of the active material within the protective silica nanoreactor enables controlled particle growth while allowing iridium(IV) oxide particle crystallization during the oxidizing thermal treatment at 800°C [28]. The synthesized material is thoroughly characterized by X-ray diffraction analysis (XRD), X-ray photoelectron spectroscopy (XPS), micro X-ray fluorescence (XRF), and high-angle annular dark and bright field scanning electron microscopy (HAADF-STEM, ABF-STEM). We employ rotating disc electrode (RDE) measurements to evaluate the OER activity of silica-free, thermally prepared TaO_x-IrO_2 electrocatalyst, and compare its performance to the bare IrO_2 (IrO_2-800°C, IrO_2-600°C) nanoparticles utilized with the same synthesis procedure and calcined at the respective temperatures as well as to the commercially available catalyst IrO_2 from Alfa Aeser (IrO_2-AA). The stability of the aforementioned catalysts is examined with a scanning flow cell (SFC) connected to the inductively coupled plasma mass spectrometer (ICP-MS), which enabled real-time potential-dependent tracking of dissolution, thus determining intrinsic stability of the catalyst expressed in the form of S-number [29]. The outcomes demonstrate that TaO_x-IrO_2 nano-electrocatalyst is a highly performing OER catalyst, possessing high OER mass activity while maintaining excellent stability.

2 | Results and Discussion

The synthesis of TaO_x-IrO_2 nanoparticles (Figure 1) employs a modified reverse microemulsion (RME) method previously reported by our group [28]. This method relies on the encapsulation of active material into a protective silica shell, which enables thermal treatment at high temperatures while preserving the particle size and morphology. Namely, two separate reverse microemulsions, RME 1 and RME 2, comprised of *n*-heptane-surfactant-water, are necessary to generate tantalum-oxyhydroxide nanoparticles ($TaO(OH)_x$) starting from tantalum ethoxide ($Ta(OC_2H_5)_5$) and iridium oxyhydroxide nanoparticles ($IrO(OH)_x$) starting from hydrated iridium(III) chloride ($IrCl_3$*nH_2O). Consequently, upon integration of the two reverse microemulsions (RME 1 and RME 2) in one unique, uniformly dispersed tantalum and iridium oxyhydroxide nanoparticles are generated followed by their encapsulation in a protective silica shell. Such encapsulated material, washed and dried, is further thermally treated in a synthetic air atmosphere at 800°C with a temperature ramp of 2°C min^{-1} and an annealing time of 5 h. The final product (TaO_x-IrO_2) is obtained after silica removal with 2.5 M NaOH solution at 70°C.

Scanning transmission electron microscopy (STEM) (Figure 2) reveals the morphology and particle size distribution of thermally treated TaO_x-IrO_2 nanoparticles. HAADF-STEM images (Figure 2a–c) show that the prepared TaO_x-IrO_2 nanoparticles are well encapsulated in the single silica shells with a mean Sauter diameter of 9.3 nm (Figure 2f, green bars). We use the Sauter mean diameter, D[3,2], as a reliable measure of particle size because it accounts for both surface area and volume, providing a representative size for processes influenced by interfacial phenomena. Secondary electron imaging of the extensive area of silica-encapsulated TaO_x-IrO_2 nanoparticles (Figure S1a–c) confirms that all active material is contained within the protective silica shell, preventing uncontrolled particle growth during thermal treatment. This finding demonstrates the exceptional capability of the silica nanoreactor in controlling both the size and morphology of synthesized nanoparticles during thermal treatment at 800°C, even in the more complex system of mixed oxide nanoparticles (TaO_x-IrO_2), as compared to previously studied thermally treated bare IrO_2 nanoparticles [28]. The inclusion of TaO_x nanoparticles alters the structural evolution observed in bare IrO_2, preventing the formation of a single central IrO_2 particle during the thermal treatment (c.f. Figure S2a,b). Instead, the IrO_2 nanoparticles remain dispersed on the pre-formed TaO_x nanoparticles. This resulted in significantly smaller IrO_2 nanoparticles in the mixed oxide system (TaO_x-IrO_2) compared to bare IrO_2 nanoparticles after the removal of silica (Figure 2d) with a mean Sauter diameter of 1.8 nm (Figure 2f, blue bars). STEM energy-dispersive X-ray spectroscopy (STEM-EDS) elemental mapping (Figure 2e) suggests the homogeneous distribution of Ta and Ir throughout the sample.

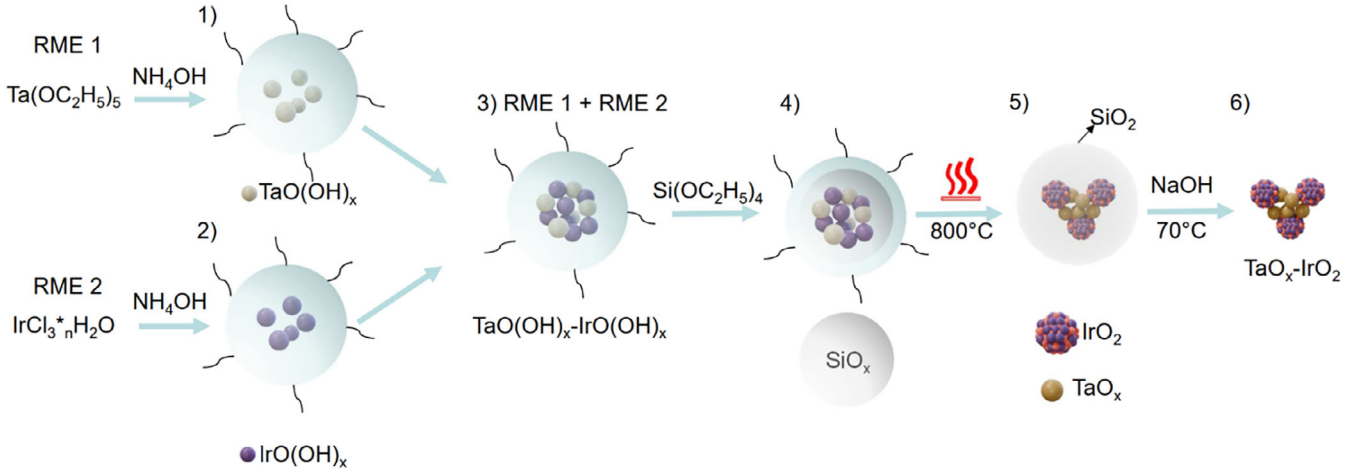

FIGURE 1 | Schematic illustration of the reverse microemulsion synthesis route for TaO_x-IrO_2 nanoparticles. (1) Hydrolysis of tantalum ethoxide in first reverse microemuslion (RME 1) leading to the formation of $TaO(OH)_x$ species. (2) Subsequent hydrolysis of hydrated iridium(III) chloride in second reverse microemulsion (RME 2) to form $IrO(OH)_x$. (3) Addition of RME 2 to RME 1 resulting in the formation of $TaO(OH)_x$ -$IrO(OH)_x$. composites. (4) Introduction of tetraethyl orthosilicate ($Si(OC_2H_5)_4$) to encapsulate the $TaO(OH)_x$-$IrO(OH)_x$ nanoparticles in a silica shell. (5) Thermal treatment at 800°C in synthetic air atmosphere to induce IrO_2 crystallization and stabilization of TaO_x and IrO_2 within the silica matrix. (6) Removal of the silica shell by NaOH treatment at 70°C to yield the final TaO_x-IrO_2 nanoparticles.

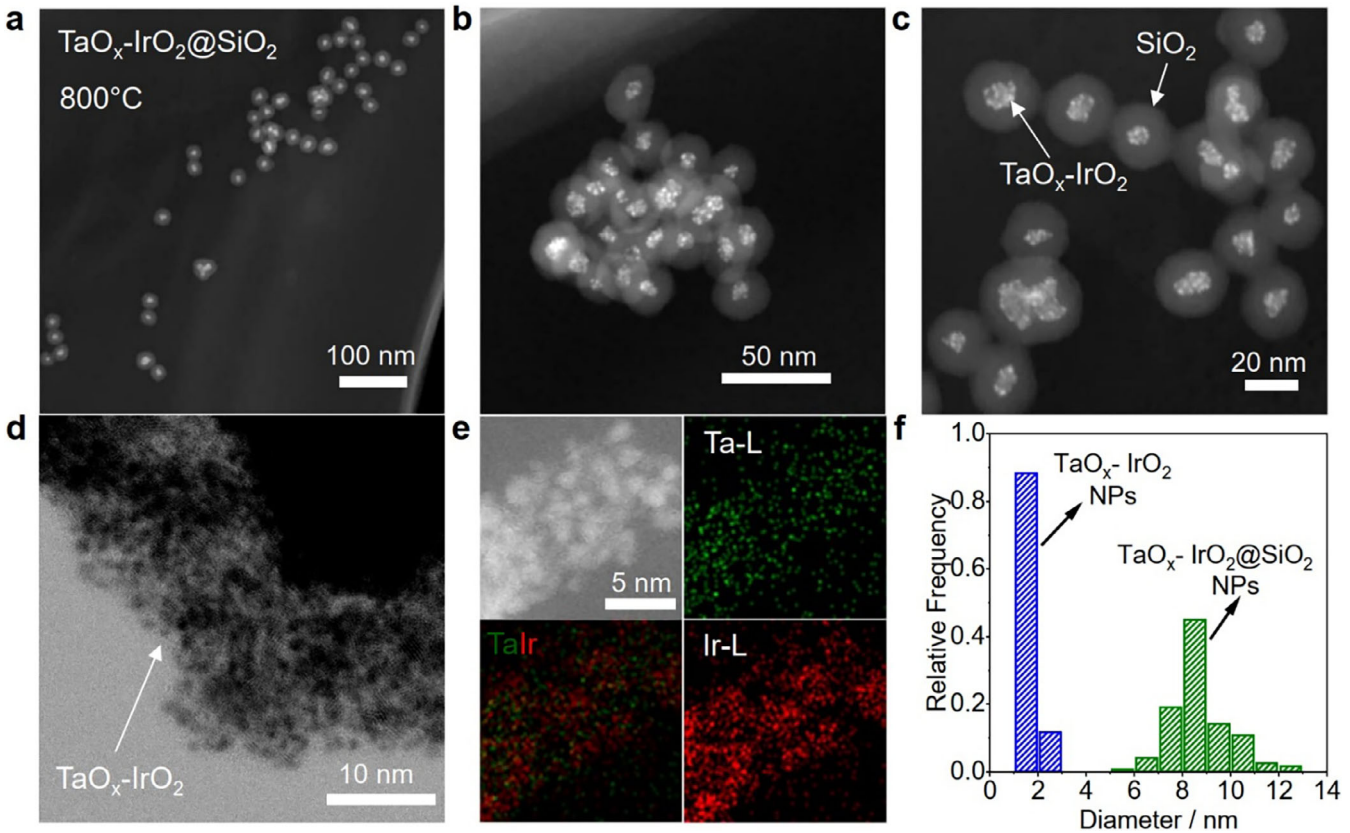

FIGURE 2 | Scanning transmission electron microscopy (STEM) high-angle annular dark (HAADF-STEM) and annular bright field (ABF-STEM) images of thermally treated (800°C) TaO_x-IrO_2 nanoparticles with the particle size distribution histograms. (a–c) Selected HAADF-STEM images of TaO_x-IrO_2 nanoparticles encapsulated in silica shell, white arrows indicating TaO_x-IrO_2 and SiO_2 phase. (d) ABF-STEM image of TaO_x-IrO_2 after removal of protective silica shell and (e) STEM energy-dispersive X-ray spectroscopy (STEM-EDS) elemental mapping of targeted nanoparticles. (f) Particle size distribution histograms, green bars relate to agglomerate size within the silica shell, while blue bars indicate the size of nanoparticles after silica removal.

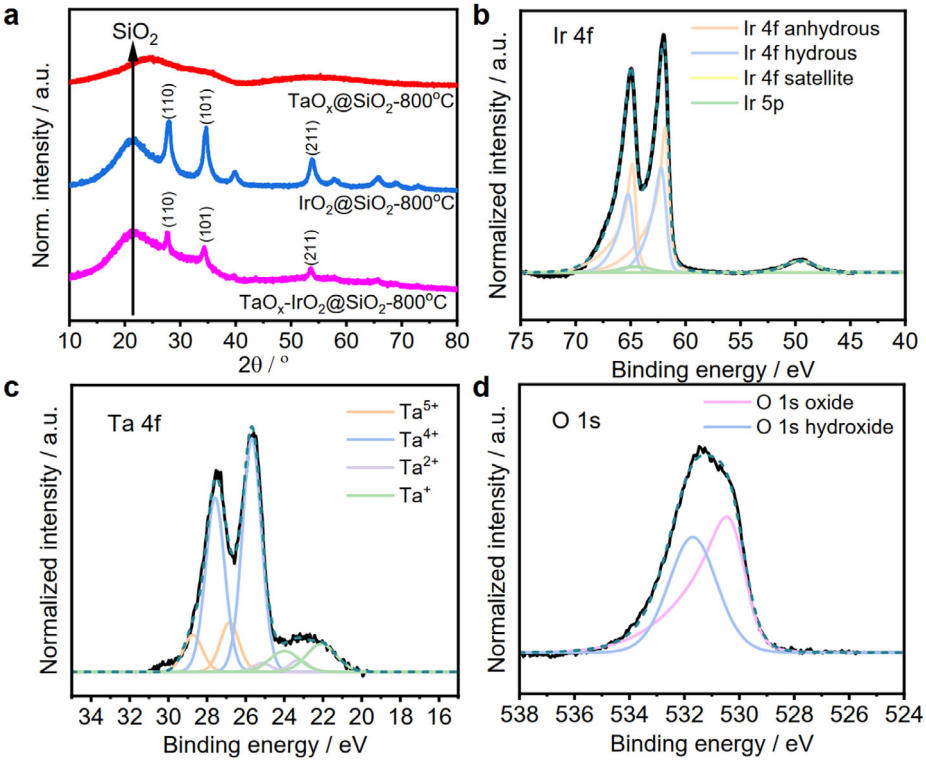

FIGURE 3 | (a) XRD patterns (Cu K_α radiation) of silica encapsulated TaO_x, IrO_2, and TaO_x-IrO_2 calcined at 800°C in synthetic air atmosphere. High-resolution XPS spectra corresponding to (b) Ir 4f, (c) Ta 4f, and (d) O 1s of silica-free TaO_x-IrO_2 catalyst calcined at 800°C.

The XRD is utilized to examine the crystal structure of the calcined TaO_x-IrO_2 sample encapsulated in a silica shell. Apart from the broad peak appearing at ~21°, which we attributed to amorphous silica (Figure 3a), the XRD data reveal a rutile crystal structure typical of IrO_2, observed also in silica encapsulated bare IrO_2 sample calcined at 800°C (IrO_2@SiO_2-800°C) (Figure 3a) [30].

To shed light on the influence of TaO_x on the sample's crystalline architecture, control experiments were conducted. TaO_x nanoparticles encapsulated in silica (TaO_x@SiO_2-800°C) were synthesized under identical conditions as the primary sample, excluding the addition of reverse microemulsion (RME 2) containing iridium-based precursor. The STEM analysis of these control nanoparticles are presented in Figure S3, which reveals the presence fo Ta and O. The XRD pattern of the TaO_x@SiO_2-800°C sample (Figure 3a) exhibits a broad, diffuse diffraction profile indicative of an amorphous structure.

Additionally, we conduct Rietveld refinement of crystalline reference samples of bare IrO_2 encapsulated in silica, which were synthesized by utilizing only RME 2 reverse microemulsion and consequently calcined at 600°C (IrO_2@SiO_2.600°C) and 800°C (IrO_2@SiO_2-800°C), and compare it to TaO_x-IrO_2@SiO_2-800°C. Rietveld refinement from TaO_x-IrO_2@SiO_2-800°C (c.f. Figure S5, Table S1), shows no discernible change in lattice parameters (i.e. values lie within the error of the analysis) compared to IrO_2@SiO_2-600°C and IrO_2@SiO_2-800°C (c.f. Figure S4, Table S1). This confirms that the rutile crystalline phase in TaO_x-IrO_2@SiO_2-800°C originates exclusively from IrO_2. Notably, the identical peak positions (i.e. 2θ diffraction angles) observed in TaO_x-IrO_2-800°C after silica removal (Figure S6) further verify the retention of the rutile crystal structure in silica-free sample. To examine the surface chemical composition and valence states of the prepared TaO_x-IrO_2 electrocatalyst, we performed XPS analysis. The XPS survey spectra (Figure S7a) confirmed the presence of Ta, Ir, and O, with no detectable Cl residues from the iridium precursor (Figure S7b). Notably, we observe no trace of Si on the sample's surface (Figure S7c), indicating successful silica removal after thermal treatment and NaOH washing. High-resolution spectra of Ir 4f core-level region (Figure 3b) show asymmetric peaks attributed to spin-orbit split components Ir $4f_{7/2}$ and Ir $4f_{5/2}$, with the binding energies of 62.0 and 65.0 eV, respectively. The slightly higher binding energy values of the examined sample compared to typically reported values for rutile-type IrO_2 (61.9, 64.9 eV) were attributed to the minor presence of Ir(III) [31]. Deconvolution of the Ta 4f spectra (Figure 3c) suggests that TaO_x is in Ta(IV) oxidation state as the binding energies of the corresponding spin-orbit split components Ta $4f_{7/2}$ and Ta $4f_{5/2}$ are 25.6 and 27.5 eV [32].

Table S2 summarizes the deconvolution details of Ta 4f and Ir 4f high-resolution spectra. For the crystalline reference samples IrO_2-600°C and IrO_2-800°C, the binding energies are 61.9 eV (Ir $4f_{7/2}$), and 64.9 eV (Ir $4f_{5/2}$) with asymmetric peak shapes closely resembling those of Ir 4f spectra of TaO_x-IrO_2-800°C (Figure S8a). In contrast, the IrO_2 reference from Alpha Aeser (IrO_2-A.A) shows broader Ir $4f_{7/2}$ and Ir $4f_{5/2}$ peaks at 62.0, 65.0 eV, indicative of a greater contribution from mixed iridium oxidation states. (c.f. Figure S8a). Consistently, XRD analysis (Figure S8b) of the IrO_2-A.A sample shows a metallic Ir peak and a broad feature attributed to amorphous IrO_2, indicating a metallic core with an

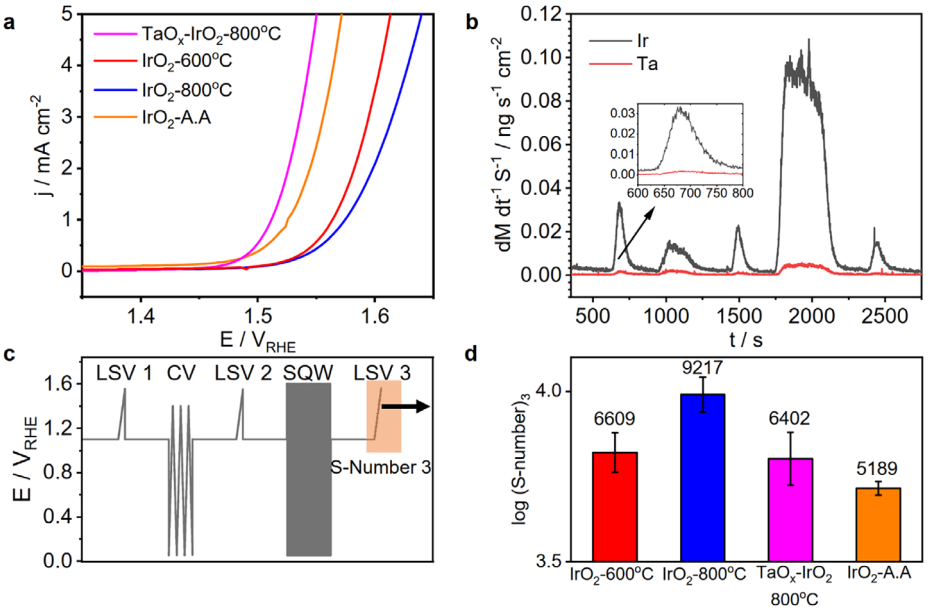

FIGURE 4 | Stability measurement of silica-free TaO_x-IrO_2 calcined at 800°C, bare IrO_2 calcined at 600°C and 800°C, and the reference IrO_2 catalyst from Alfa Aeser measured with a SFC coupled to an ICP-MS in 0.1 M $HClO_4$. (a) Linear sweep voltammograms (LSVs) of analyzed samples taken with a scan rate of 10 mV s^{-1}. (b) Exemplar dissolution profile of tantalum and iridium from TaO_x-IrO_2 catalyst calcined at 800°C. (c) Stability assessment protocol. (d) S-number (S-Number 3, orange box) was determined during the third LSV for all analyzed samples.

amorphous oxide layer on the surface of the commercial catalyst. The corresponding HAADF-STEM images of IrO_2-A.A can be found in Figure S11.

The XPS spectra of O 1s (Figure 3d) we deconvoluted (c.f Table S3) via two contributing peaks belonging to lattice oxygen at 530.2 eV and oxygen from the hydroxyl group at 531.7 eV, contributing with 57.2% and 42.8%, respectively. The significant surface coverage with hydroxyl groups indicates the presence of oxygen defects and is often correlated with enhanced OER activity of electrocatalysts [33, 34]. In a recent study, Wang et al., also observed the increased fraction of hydroxyl groups on the surface of IrO_2@TaO_x@TaB when the Ir content was above 30 wt.% compared to the bare IrO_2 catalyst [35].

Given that research on OER catalysts has typically prioritized activity over long-term durability, understanding the stability-activity relationship is essential for optimizing both performance and longevity [36]. Most reported highly active iridium-oxide-based catalysts are obtained at mild to medium temperatures (up to 400°C), resulting in structures with lower crystallinity, which in turn affects the stability as often the inverse trend between activity and stability is observed [27, 28, 36]. To do a relevant comparison of the stability performance of TaO_x-IrO_2 electrocatalyst calcined at 800°C (TaO_x-IrO_2-800°C), we investigated IrO_2-600°C, IrO_2-800°C, and IrO_2-AA under the same conditions, using a scanning flow cell coupled with ICP-MS. This method enabled us to track in situ potential-dependent dissolution (Figure 4a–d) under OER-relevant conditions. To gain a trustworthy stability comparison between analyzed catalysts, we utilized the S-number [29], a metric obtained by dividing the amount of generated oxygen, n(O_2) and the corresponding amount of dissolved iridium, n(Ir). Although the S-number represents the intrinsic value of the catalyst's stability, we avoid including benchmark S-number values reported in the literature due to its sensitivity to the applied electrochemical protocol, experimental setup (aqueous model system or membrane electrode assembly), and reaction environment, consequently yielding orders of magnitude different S-number values throughout the literature for the same catalyst [37]. In this study, the S-number is calculated by obtaining n(O_2), n(Ir) values during the last linear sweep voltammogram step (LSV 3) of the electrochemical protocol (Figure 4c, Table S6). As shown in Figure 4d, the stability of TaO_x-IrO_2-800°C is comparable to that of bare IrO_2-600°C and exceeds that of commercial IrO_2 (IrO_2-AA), though it remains lower than the stability of IrO_2-800°C. However, the polarization curves recorded during the stability assessment (Figure 4a) reveal a clear difference in onset potential between TaO_x-IrO_2-800°C and the most stable IrO_2-800°C, which highlights the activity trend discussed in the following section [26]. Moreover, a significantly lower dissolution rate of tantalum, exhibited as more than a 13-fold reduction compared to iridium during the initial LSV cycle (Figure 4b), suggests that tantalum oxide is a promising support material.

The electrocatalytic activity (Figure 5a–c, Table S4) of the calcined TaO_x-IrO_2 electrocatalyst toward the oxygen evolution reaction (OER) was assessed in 0.1 M $HClO_4$ using a three-electrode rotating disc electrode (RDE) setup and compared to OER activity of IrO_2-600°C, IrO_2-800°C, and IrO_2-A.A. As shown in Figure 5b, we highlight the OER polarization curves of the respective catalysts normalized to the total iridium loading within the OER-relevant potential window. For this purpose, we determined the iridium content in TaO_x-IrO_2 after silica removal to be 72 wt% (c.f. Figure S9). The TaO_x-IrO_2 catalyst exhibits remarkable performance, with an average OER mass activity of 337 mA mg_{Ir}^{-1} at 1.53 V_{RHE} (Figure 5c), surpassing IrO_2-AA by more than two-fold. It also demonstrates significantly higher activity compared

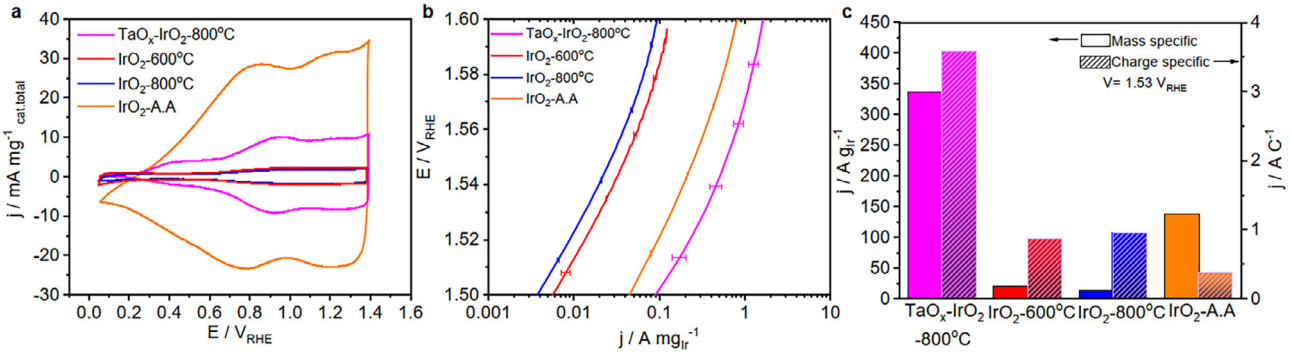

FIGURE 5 | RDE measurements of silica-free TaO_x-IrO_2, bare IrO_2 calcined at 600°C, and 800°C, and the reference IrO_2 catalyst from Alfa Aeser in 0.1 M N_2-saturated $HClO_4$. (a) Cyclic voltammetry measured with a scan rate of 50 mV s^{-1} between 0.05 and 1.4 V_{RHE}. The current density is normalized to the total amount of catalyst. (b) OER mass activities (normalized to Ir amount) obtained from the first linear sweep voltammetry (LSV) (iR drop corrected) scanning between 1.3 and 1.6 V_{RHE} (highlighted potential region from 1.5 V_{RHE} to 1.6 V_{RHE}) with a scan rate of 10 mV s^{-1} and forced convection at 900 rpm. (c) Comparison of mass specific and charge specific OER activities at 1.53 V_{RHE}.

to its bare counterparts, IrO_2-600°C and IrO_2-800°C. The reason for such discrepancy in OER activities, especially between TaO_x-IrO_2-800°C and bare IrO_2-600°C, and IrO_2-800°C is arguably due to the difference in structural evolution during the synthesis i.e. the generation of smaller IrO_2 nanoparticles, induced by the presence of TaO_x [25, 28, 30]. The charge-specific OER activities at 1.53 V_{RHE} (Figure 5c), derived from the pseudocapacitive region of the cyclic voltammograms (c.f. Figure S10) reveal that TaO_x-IrO_2 synthesized at 800°C exhibits nearly an order of magnitude higher charge-specific activity than IrO_2-A.A and more than four times higher charge-specific activity compared to IrO_2-600°C. At the same time, the S-number of TaO_x-IrO_2-800°C is comparable to that of IrO_2-600°C and superior to IrO_2-A.A, highlighting the significant impact of TaO_x on the performance and stability of IrO_2 in OER applications. Despite the high temperatures, the cyclic voltammogram of TaO_x-IrO_2-800°C (Figure 5a) reveals the features typical of highly active hydrous iridium-oxide, similar to the IrO_2-A.A, but with lower pseudocapacitive charge, presumably due to higher annealing temperature during the synthesis [9]. The hydrous nature of the TaO_x-IrO_2-800°C surface is corroborated by the presence of hydroxyl species observed in the XPS O 1s spectrum. The deprotonation of these hydroxyl species during the oxidizing potentials is shown to trigger the catalyst OER activity [33]. The potential synergetic effect between OER-inactive TaO_x and IrO_2 caused by plausible electronic interaction between the two oxide materials, may also contribute to the high OER activity of TaO_x-IrO_2-800°C [11, 13, 38]. In Table S5, we compare the OER mass activities of several state-of-the-art catalysts with similar chemical compositions. The TaO_x-IrO_2-800°C catalyst shows competitive performance with highly active sub-2 nm IrO_2 from Zheng et al. [25], IrO_2-Ta_2O_5 (7:3) [22] and outperforms IrO_2@TaO_x@TaB [35], while only mass selected $Ir_{0.1}Ta_{0.9}O_{2.45}$ [25] is more active. These results further highlight the strong activity of TaO_x-IrO_2-800°C among advanced OER catalysts.

3 | Conclusion

In this study, we have successfully synthesized a structurally ordered and size-controlled OER catalyst based on TaO_x-IrO_2 nanoparticles calcined at 800°C. Introducing TaO_x as a matrix not only lowered the content of scarce iridium but has also influenced the structural evolution of the material during the thermal treatment while protected within a silica shell, resulting in a material with a significantly higher surface-to-volume ratio compared to the structural evolution of bare IrO_2 under the same synthesis conditions. Such thermally prepared TaO_x-IrO_2 electrocatalyst exhibits superior mass OER activity that outpeforms some of the most active recently reported state-of-the-art catalysts based on similar chemical composition. Notably, TaO_x-IrO_2 synthesized at 800°C outperformed the reference IrO_2 catalyst (IrO_2-A.A) with 2.5 time's higher mass activity and nearly tenfold higher charge-specific activity. Additionally, it exhibited superior intrinsic stability, as indicated by the S-number metric, underscoring the significant impact of TaO_x on enhancing both the activity and stability of IrO_x. The ability to perform the controlled thermal treatment at 800°C maximized the catalyst resistance toward dissolution. Besides, remarkably low dissolution of tantalum during the stability assessment protocol highlights the importance of material choice when designing novel OER catalysts. Potential beneficial interaction between TaO_x and IrO_2 could have additionally contributed to the overall improvement of catalyst electrochemical performance, advocating the OER catalyst design strategy based on mixed oxide approach.

4 | Experimental Section

4.1 | Synthesis

4.1.1 | Chemicals

n-heptane (99+%, Extra Dry, Thermo Scientific Chemicals), water (D.I.), Brij L4 (Mn ~362, Sigma Aldrich), Ammonia (28%–30%, Sigma Aldrich), Tetraethyl Orthosilicate (Thermo Scientific Acros), Methanol, Acetone, Sodium hydroxide pellets (AppliChem GmbH), tantalum(V)-ethoxide (99.98% trace metals basis, Sigma Aldrich), iridium(III)-chloride hydrate (Sigma Aldrich), IrO_2 (Premion, Alfa Aeser).

4.1.2 | TaO_x-IrO_2@SiO_2 Synthesis Procedure

Before forming a reverse microemulsion, hydrolysis of the hydrated iridium(III)-chloride is done by preparing 0.07 mmol

per milliliter iridium solution comprising a mixture of 4.3 mL of ultra-pure water and 0.7 mL ammonia (28%–30%) aqueous solution. The solution is stirred at ambient conditions ($T = 298$ K) in the vial with a closed lid until the formation of a clear purple solution indicating the formation of iridium(IV) oxyhydroxide.

For the purpose of TaO_x synthesis, a dry round bottom flask (50 mL) is coupled to the Schlenk line and flushed with nitrogen. Consequently, 25 mL of extra dry n-heptane is added in which 25 µL of tantalum (V)-ethoxide is carefully dissolved. In a separate (500 mL) round bottom flask 23 mL of Brij L4 surfactant is dispersed in 175 mL n-heptane by stirring for 10 min and additionally by ultrasonication. First reverse microemulsion (RME 1) is formed by the addition of 5 mL of water (D.I.) and 2.5 mL of ammonium hydroxide. Using the syringe, the tantalum-containing solution is transferred from the Schlenk flask to the reverse microemulsion within the time interval of 5 min and stirred under ambient conditions for 2 h.

In the meantime, a second, iridium-containing reverse microemulsion (RME 2) is prepared by dispersing 3.6 mL Brij L4 surfactant in 23 mL of n-heptane and the consequent addition of 1 mL of iridium (IV) oxyhydroxide solution. After 2 h of RME 1 stirring, RME 2 is dropwise added to RME 1 via a 50 mL syringe coupled to a Ø 0.6 mm cannula, and the final reverse microemulsion consisting of the RME 1 and RME 2 is stirred for another 2 h. Lastly, 0.75 mL of Tetraethyl Orthosilicate is added to the final reverse microemulsion and left to react overnight (≈ 16 h).

After stirring overnight to induce particle precipitation, 150 mL of methanol is added, followed by vigorous stirring for a few minutes. The mixture is then allowed to settle for 30 min to complete the precipitation process. At this stage, three distinct phases form: an upper n-heptane-rich layer, a middle methanol layer, and a bottom layer where the fluffy, light purple precipitate settles. The upper layer is decanted and the leftover slurry is centrifuged and washed subsequently with methanol and acetone respectively. The obtained solid phase is dried under vacuum at 60°C for 1 h and prepared for thermal treatment. In total, 220 mg of dry product is obtained. Thermal treatment is done in a tubular furnace under a synthetic air atmosphere at a flow rate of 10 Nl h^{-1} with a temperature ramp of 2°C min^{-1} and 5 h of annealing time at 800°C.

The removal of silica is done under reflux at 70°C by dispersing calcined product in 30 mL of 2.5 M NaOH solution for 20 h. The resulting dispersion is then centrifuged and washed with D.I. water until neutral pH. The black resulting dry powder represents TaO_x-IrO_2 nanoparticles.

4.1.3 | SFC-ICP-MS

4.1.3.1 | Electrode Preparation. Electrodes with a constant total catalyst loading of 20 µg cm^{-2} and 20 wt% Nafion content were prepared by drop-casting 0.2 µL of ink on polished glassy carbon plates (SIGRADUR G, HTW). The drop-casted electrodes were examined with a Keyence VK-X250 confocal laser-scanning microscope to ensure comparable size (roughly 1.3 mm diameter) and quality of the electrode spots.

The silica-free inks were prepared by suspending the investigated catalyst powders in DI H_2O (Merck Milli-Q) and adding 2-propanol for stabilization. Nafion perfluorinated resin solution (Alfa Aesar, 5 wt%) was added afterward to adjust the adhesion of the spots to the glassy carbon substrate. Solvent content of the Nafion solution was accounted for to achieve a mixture of 7/8 H_2O and 1/8 2-propanol. Prior to drop-casting, the inks were sonicated for 15 min, and the pH was adjusted to 11 by adding 1 M KOH to achieve homogeneity.

4.1.3.2 | Dissolution Measurements. The SFC-ICP-MS setup with an opening diameter of 2 mm was used as described in prior publications [29, 39]. Fresh 0.1 M $HClO_4$ (Merck Suprapur 70% $HClO_4$) was prepared daily by mixing stock solution and DI H_2O. The electrochemical measurements were carried out with Ar-purged 0.1 M $HClO_4$ at a flow rate of 207 µL min^{-1}, connecting the SFC directly to a NexIon 350 spectrometer (Perkin Elmer). A saturated Ag/AgCl reference (Metrohm) and a graphite rod counter electrode were used for measurements. To ensure the constant performance of the ICP-MS, an internal standard solution (10 µg L^{-1} 187Re in 0.1 M $HClO_4$) was added downstream towards the ICP-MS. 4-point calibration curves were recorded daily by measuring freshly prepared solutions of known Ir- and Ta-content (0, 0.5,1.0, 5.0 µg L^{-1} in 0.1 M $HClO_4$).

4.1.4 | RDE

The catalyst films for electrochemical activity measurements in the liquid half-cell were prepared by dispersing the investigated catalyst in water (ultrapure grade, VWR) with an ultra-sonic horn (Branson Sonifier), pulse mode at 35% intensity for 30 min onto a glassy carbon electrode (Ø 5 mm) of the RDE tip. The electrodes with a constant catalyst loading (total catalyst mass) of 0.05 mg cm^{-2} were prepared by drop-casting of 15 µL of ink on a polished glassy carbon RDE tip. The drop-casted inks were then dried under a constant stream of Argon at room temperature. All the measurements were conducted at room temperature in a multi-neck glass cell in 0.1 M $HClO_4$ (Rotipuran Ultra 70%, Carl Roth GmbH) purged with a constant flow of nitrogen. A saturated Ag/AgCl reference electrode (3 M KCl, Metrohm) and a graphite rod counter electrode were used. The setups were equipped with a Gamry Reference 600 potentiostat and a Radiometer Analytical rotation controller.

4.2 | Characterization Methods

4.2.1 | XRD Analysis

A Bruker D2 Phaser second Generation was used with a wavelength of Cu $K_\alpha = 1.5406$ Å. Measurements were taken in a 2-theta range from 5° to 90° with a measurement speed of 0.02° $(2\ s)^{-1}$ using a background-free silicon sample holder.

4.2.2 | HAADF-STEM Measurements

HAADF-STEM micrographs were obtained using a JEM2100F (JEOL) microscope (200 kV, ZnO/W(100)-emitter). The samples were prepared by dispersion of the investigated material in

ethanol with ultra-sonication. Subsequently, 3×10 µL of resulting dispersion was drop casted onto a Lacey–Carbon coated gold or copper grid.

4.2.3 | HR-STEM Measurements

The HR-STEM measurements were conducted on a Hitachi HF5000 environmental STEM at 80 kV acceleration voltage. The system is equipped with a cold field emission electron gun, a Cs probe corrector (Hitachi), an energy dispersive spectroscopy unit (two Oxford Instruments Aztec Energy TEM Advanced EDX System Ultim TLE detectors, 100 mm^2 active area with a 2 sr solid angle), a post-column energy filter system (CEOS CEFID), and a TVIPS TemCam XF416 camera. To enable energy-filtered 4D STEM measurements, the microscope is equipped with a MerlinEM Direct Electron Detector (QuantumDetectors). The HF5000 is equipped with an Everhart–Thornley detector for imaging the surface topography using secondary electrons. After drop-casting 10 µL of the catalyst suspension on a MEMS heating chip (Norcada), the MEMS chip was dried in a vacuum drying oven under reduced pressure (2×10^{-2} mbar) at 75°C for 18 h. With a Hitachi single tilt heating holder, the chip was transferred to the microscope. heated to 200°C for 30 min to remove organic contaminations. To mitigate beam damage, EDX maps with a resolution of 512×512, a pixel dwell time of 5 µs and a frame count of 600 were recorded.

4.2.4 | XPS Analysis

All XPS measurements were performed using a SPECS instrument. The samples were excited with monochromatic AI K_α radiation at 1486.74 eV. The emitted photoelectrons were collected using a 150 mm hemispherical energy analyzer (Phoibos 150, SPECS). For each sample a survey scan with a pass energy of 20 eV and high-resolution C 1s, O 1s, Cl 2p, Si 2s, Ir 4p, Ir 4d, Ir 4f, and Ta 4f regions with a pass energy of 10 eV were measured. The adventitious C 1s signal of carbon was used for binding energy calibration and assigned to 284.7 eV. The samples were prepared by drop-casting 10 µL of water-based ink of the respective sample (concentration 6.5 mg mL^{-1}) on 1×1 cm^2 glassy carbon plates. All XPS spectra were deconvoluted using CasaXPS peak fitting software [40].

4.2.5 | Micro X-Ray Fluorescence Analysis

The element concentrations of samples were collected by Bruker M4 TORNADO. Approximately 2 mg of each sample was placed on a titanium sheet and analyzed under a vacuum pressure of 20 mbar. The measurements were performed using a source voltage of 50 kV and a current of 600 µA. The X-ray source in the M4 TORNADO system consists of a 30 W metal-ceramic tube with a rhodium (Rh) anode.

Author Contributions

Marko Malinovic: conceived the manuscript, performed material synthesis, RDE measurements, HAADF-STEM measurements, discussed the results, and assisted during manuscript preparation; **Marc Ledendecker**: conceived the manuscript, discussed the results, and assisted during manuscript preparation; **Moritz Geuß**: performed SFC ICP-MS measurements, data analysis, discussed the results, and assisted during manuscript preparation; **Serhiy Cherevko**: performed SFC ICP-MS measurements, data analysis, discussed the results, and assisted during manuscript preparation; **Paul Paciok**: performed HR-STEM experiments, discussed the results, and assisted during manuscript preparation; **Marc Heggen**: performed HR-STEM experiments, discussed the results, and assisted during manuscript preparation; **Jisik Choi**: performed XPS measurements, data analysis, discussed the results, and assisted during manuscript preparation; **Huize Wang**: performed XRF measurement, discussed the results and assisted during manuscript preparation; **Souriddha Sanyal**: performed the XRD analysis, discussed the results and assisted during manuscript preparation.

Acknowledgments

MM, JC, SS, PP and ML acknowledge the Federal Ministry of Education and Research (BMBF) in the framework of NanoMatFutur (SynKat, FK: 03XP0265) for financial support. HW and ML acknowledge the Initiative and Networking Fund of the Helmholtz Association for funding. Marko Malinovic also acknowledges the efforts of Hannah Lamers and Sun-Myung Kim for XRD and XPS data acquisition.

Open access funding enabled and organized by Projekt DEAL.

Conflicts of Interest

The authors declare no conflicts of interest.

Funding Sources

Federal Ministry of Education and Research (BMBF) in the framework of NanoMatFutur (SynKat, FK: 03XP0265).

Data Availability Statement

The data that support the findings of this study are available from the corresponding author upon reasonable request.

References

1. M. Clapp, C. M. Zalitis, and M. Ryan, "Perspectives on Current and Future Iridium Demand and Iridium Oxide Catalysts for PEM Water Electrolysis," *Catalysis Today* 420 (2023): 114140, https://doi.org/10.1016/j.cattod.2023.114140.

2. S. Kiemel, T. Smolinka, F. Lehner, J. Full, A. Sauer, and R. Miehe, "Critical Materials for Water Electrolysers at the Example of the Energy Transition in Germany," *International Journal of Energy Research* 45 (2021): 9914–9935, https://doi.org/10.1002/er.6487.

3. P. L. Cabot, M. V. Martínez-Huerta, and F. Alcaide, "Advanced Supports for Noble Metal Catalysts in Proton Exchange Membrane Water Electrolysers: A Review," *Johnson Matthey Technology Review* 67 (2023): 249–265, https://doi.org/10.1595/205651323X16648726195503.

4. M. Bernt, A. Hartig-Weiß, and M. F. Tovini, "Current Challenges in Catalyst Development for PEM Water Electrolyzers," *Chemie Ingenieur Technik* 92 (2020): 31–39, https://doi.org/10.1002/cite.201900101.

5. M. Bernt, A. Siebel, and H. A. Gasteiger, "Analysis of Voltage Losses in PEM Water Electrolyzers with Low Platinum Group Metal Loadings," *Journal of The Electrochemical Society* 165 (2018): F305, https://doi.org/10.1149/2.0641805jes.

6. M. Bernt and H. A. Gasteiger, "Influence of Ionomer Content in IrO_2 /TiO_2 Electrodes on PEM Water Electrolyzer Performance," *Journal of*

The Electrochemical Society 163 (2016): F3179, https://doi.org/10.1149/2.0231611jes.

7. A. Buttler and H. Spliethoff, "Current Status of Water Electrolysis for Energy Storage, Grid Balancing and Sector Coupling via Power-to-Gas and Power-to-Liquids: A Review," *Renewable and Sustainable Energy Reviews* 82 (2018): 2440–2454, https://doi.org/10.1016/j.rser.2017.09.003.

8. O. Kasian, S. Geiger, and T. Li, "Degradation of Iridium Oxides via Oxygen Evolution from the Lattice: Correlating Atomic Scale Structure with Reaction Mechanisms," *Energy & Environmental Science* 12 (2019): 3548–3555, https://doi.org/10.1039/C9EE01872G.

9. S. Geiger, O. Kasian, B. R. Shrestha, A. M. Mingers, K. J. J. Mayrhofer, and S. Cherevko, "Activity and Stability of Electrochemically and Thermally Treated Iridium for the Oxygen Evolution Reaction," *Journal of The Electrochemical Society* 163 (2016): F3132–F3138, https://doi.org/10.1149/2.0181611jes.

10. L. C. Seitz, C. F. Dickens, and K. Nishio, "A Highly Active and Stable IrO_X /$SrIrO_3$ Catalyst for the Oxygen Evolution Reaction," *Science* 353 (2016): 1011–1014, https://doi.org/10.1126/science.aaf5050.

11. N. Zhang, J. Du, and N. Zhou, "High-valence Metal-doped Amorphous IrO as Active and Stable Electrocatalyst for Acidic Oxygen Evolution Reaction," *Chinese Journal of Catalysis* 53 (2023): 134–142, https://doi.org/10.1016/S1872-2067(23)64517-6.

12. B. Han, M. Risch, and S. Belden, "Screening Oxide Support Materials for OER Catalysts in Acid," *Journal of The Electrochemical Society* 165 (2018): F813, https://doi.org/10.1149/2.0921810jes.

13. A. Hartig-Weiss, M. Miller, and H. Beyer, "Iridium Oxide Catalyst Supported on Antimony-Doped Tin Oxide for High Oxygen Evolution Reaction Activity in Acidic Media," *ACS Applied Nano Materials* 3 (2020): 2185–2196, https://doi.org/10.1021/acsanm.9b02230.

14. E. Kolle-Görgen, G. Fortunato, and M. Ledendecker, "Catalyst Stability in Aqueous Electrochemistry," *Chemistry of Materials* 34 (2022): 10223–10236, https://doi.org/10.1021/acs.chemmater.2c02443.

15. Y.-T. Kim, P. P. Lopes, and S.-A. Park, "Balancing Activity, Stability and Conductivity of Nanoporous Core-Shell Iridium/Iridium Oxide Oxygen Evolution Catalysts," *Nature Communications* 8 (2017): 1449, https://doi.org/10.1038/s41467-017-01734-7.

16. E. Oakton, D. Lebedev, and M. Povia, "IrO_2 -TiO_2: A High-Surface-Area, Active, and Stable Electrocatalyst for the Oxygen Evolution Reaction," *ACS Catalysis* 7 (2017): 2346–2352, https://doi.org/10.1021/acscatal.6b03246.

17. G. C. da Silva, S. I. Venturini, and S. Zhang, "Oxygen Evolution Reaction on Tin Oxides Supported Iridium Catalysts: Do We Need Dopants?," *ChemElectroChem* 7 (2020): 2330–2339, https://doi.org/10.1002/celc.202000391.

18. S. Geiger, O. Kasian, A. M. Mingers, K. J. J. Mayrhofer, and S. Cherevko, "Stability Limits of Tin-based Electrocatalyst Supports," *Scientific Reports* 7 (2017): 4595, https://doi.org/10.1038/s41598-017-04079-9.

19. Z. Fang, Z. Tang, and S. Lin, "Doped TiO_2 -supported IrO_2 Electrocatalysts with High Activity and Durability toward the Acidic Oxygen Evolution Reaction," *CrystEngComm* 26 (2024): 475–483, https://doi.org/10.1039/D3CE01036H.

20. H. P. Tran, H. N. Nong, and H.-S. Oh, "Catalyst–Support Surface Charge Effects on Structure and Activity of IrNi-Based Oxygen Evolution Reaction Catalysts Deposited on Tin-Oxide Supports," *Chemistry of Materials* 34 (2022): 9350–9363, https://doi.org/10.1021/acs.chemmater.2c01098.

21. W. Hu, S. Chen, and Q. Xia, "IrO_2/Nb–TiO_2 Electrocatalyst for Oxygen Evolution Reaction in Acidic Medium," *International Journal of Hydrogen Energy* 39 (2014): 6967–6976, https://doi.org/10.1016/j.ijhydene.2014.02.114.

22. H. Li, Y. Pan, and L. Wu, "Highly Active and Stable IrO_2 and IrO_2–Ta_2O_5 Catalysts for Oxygen Evolution Reaction," *International Journal of Hydrogen Energy* 48 (2023): 26021–26031, https://doi.org/10.1016/j.ijhydene.2023.03.360.

23. V. K. Puthiyapura, S. Pasupathi, H. Su, X. Liu, B. Pollet, and K. Scott, "Investigation of Supported IrO_2 as Electrocatalyst for the Oxygen Evolution Reaction in Proton Exchange Membrane Water Electrolyser," *International Journal of Hydrogen Energy* 39 (2014): 1905–1913, https://doi.org/10.1016/j.ijhydene.2013.11.056.

24. W. Xu, G. M. Haarberg, and S. Sunde, "Calcination Temperature Dependent Catalytic Activity and Stability of IrO_2 –Ta $_2O_5$ Anodes for Oxygen Evolution Reaction in Aqueous Sulfate Electrolytes," *Journal of The Electrochemical Society* 164 (2017): F895, https://doi.org/10.1149/2.0061710jes.

25. Y.-R. Zheng, J. Vernieres, and Z. Wang, "Monitoring Oxygen Production on Mass-selected Iridium–tantalum Oxide Electrocatalysts," *Nature Energy* 7 (2022): 55–64, https://doi.org/10.1038/s41560-021-00948-w.

26. H.-S. Oh, H. N. Nong, and T. Reier, "Electrochemical Catalyst–Support Effects and Their Stabilizing Role for IrO_X Nanoparticle Catalysts during the Oxygen Evolution Reaction," *Journal of the American Chemical Society* 138 (2016): 12552–12563, https://doi.org/10.1021/jacs.6b07199.

27. D. Böhm, M. Beetz, C. Gebauer, et al., "Highly Conductive Titania Supported Iridium Oxide Nanoparticles With Low Overall Iridium Density as OER Catalyst for Large-Scale PEM Electrolysis," *Applied Materials Today* 24 (2021): 101134.

28. M. Malinovic, P. Paciok, and E. S. Koh, "Size-Controlled Synthesis of IrO_2 Nanoparticles at High Temperatures for the Oxygen Evolution Reaction," *Advanced Energy Materials* 13 (2023): 2301450, https://doi.org/10.1002/aenm.202301450.

29. S. Geiger, O. Kasian, and M. Ledendecker, "The Stability Number as a Metric for Electrocatalyst Stability Benchmarking," *Nature Catalysis* 1 (2018): 508–515, https://doi.org/10.1038/s41929-018-0085-6.

30. D. F. Abbott, D. Lebedev, and K. Waltar, "Iridium Oxide for the Oxygen Evolution Reaction: Correlation between Particle Size, Morphology, and the Surface Hydroxo Layer from Operando XAS," *Chemistry of Materials* 28 (2016): 6591–6604, https://doi.org/10.1021/acs.chemmater.6b02625.

31. S. J. Freakley, J. Ruiz-Esquius, and D. J. Morgan, "The X-Ray Photoelectron Spectra of Ir, IrO_2, and $IrCl_3$ Revisited," *Surface and Interface Analysis* 49 (2017): 794–799, https://doi.org/10.1002/sia.6225.

32. R. Simpson, R. G. White, J. F. Watts, and M. A. Baker, "XPS Investigation of Monatomic and Cluster Argon Ion Sputtering of Tantalum Pentoxide," *Applied Surface Science* 405 (2017): 79–87, https://doi.org/10.1016/j.apsusc.2017.02.006.

33. R. V. Mom, L. J. Falling, and O. Kasian, "Operando Structure–Activity–Stability Relationship of Iridium Oxides during the Oxygen Evolution Reaction," *ACS Catalysis* 12 (2022): 5174–5184, https://doi.org/10.1021/acscatal.1c05951.

34. C. Wang, A. Schechter, and L. Feng, *Nano Research Energy* (2023), https://doi.org/10.26599/NRE.2023.9120056.

35. Y. Wang, Z. Zhao, and X. Liang, "Supported IrO2 Nanocatalyst with Multilayered Structure for Proton Exchange Membrane Water Electrolysis," *Advanced Materials* 36 (2024): 2407717, https://doi.org/10.1002/adma.202407717.

36. S. H. Chang, J. G. Connell, and N. Danilovic, "Activity–stability Relationship in the Surface Electrochemistry of the Oxygen Evolution Reaction," *Faraday Discussions* 176 (2014): 125–133, https://doi.org/10.1039/C4FD00134F.

37. J. Edgington and L. C. Seitz, "Advancing the Rigor and Reproducibility of Electrocatalyst Stability Benchmarking and Intrinsic Material Degradation Analysis for Water Oxidation," *ACS Catalysis* 13 (2023): 3379–3394, https://doi.org/10.1021/acscatal.2c06282.

38. R. V. Genova-Koleva, F. Alcaide, and G. Álvarez, "Supporting IrO_2 and IrRuO Nanoparticles on TiO_2 and Nb-doped TiO_2 Nanotubes as Electrocatalysts for the Oxygen Evolution Reaction," *Journal of Energy*

Chemistry 34 (2019): 227–239, https://doi.org/10.1016/j.jechem.2019.03.008.

39. S. O. Klemm, A. A. Topalov, C. A. Laska, and K. J. J. Mayrhofer, "Coupling of a High Throughput Microelectrochemical Cell with Online Multielemental Trace Analysis by ICP-MS," *Electrochemistry Communications* 13 (2011): 1533–1535, https://doi.org/10.1016/j.elecom.2011.10.017.

40. N. Fairley, V. Fernandez, and M. Richard-Plouet, "Systematic and Collaborative Approach to Problem Solving Using X-ray Photoelectron Spectroscopy," *Applied Surface Science Advances* 5 (2021): 100112, https://doi.org/10.1016/j.apsadv.2021.100112.

Supporting Information

Additional supporting information can be found online in the Supporting Information section.

Supporting File: cctc70546-sup-0001-SuppMat.docx.